

This is the accepted manuscript made available via CHORUS. The article has been published as:

# Helical antiferromagnetic ordering in $\text{Lu}_{1-x}\text{Sc}_x\text{MnSi}$

R. J. Goetsch, V. K. Anand, and D. C. Johnston

Phys. Rev. B **90**, 064415 — Published 15 August 2014

DOI: [10.1103/PhysRevB.90.064415](https://doi.org/10.1103/PhysRevB.90.064415)

# Cycloidal Antiferromagnetic Ordering in $\text{Lu}_{1-x}\text{Sc}_x\text{MnSi}$ ( $x = 0, 0.25, 0.5$ )

R. J. Goetsch, V. K. Anand,\* and D. C. Johnston†

Ames Laboratory and Department of Physics and Astronomy, Iowa State University, Ames, Iowa 50011, USA

(Dated: July 7, 2014)

Polycrystalline samples of  $\text{Lu}_{1-x}\text{Sc}_x\text{MnSi}$  ( $x = 0, 0.25, 0.5$ ) are studied using powder x-ray diffraction, heat capacity  $C_p$ , magnetization, magnetic susceptibility  $\chi$ , and electrical resistivity  $\rho$  measurements versus temperature  $T$  and magnetic field  $H$ . This system crystallizes in the primitive orthorhombic  $\text{TiNiSi}$ -type structure (space group  $Pnma$ ) as previously reported. The  $\rho(T)$  data indicate metallic behavior. The  $C_p(T)$ ,  $\chi(T)$ , and  $\rho(T)$  measurements consistently indicate long-range antiferromagnetic (AF) transitions with AF ordering temperatures  $T_N = 246, 215$  and  $188$  K for  $x = 0, 0.25$  and  $0.5$ , respectively. A second transition is observed at somewhat lower  $T$  for each sample from the  $\chi(T)$  and  $\rho(T)$  measurements, which we speculate are due to spin reorientation transitions; these second transitions are completely suppressed in  $H = 5.5$  T. The  $C_p$  data below  $10$  K for each composition indicate an enhanced Sommerfeld electronic heat capacity coefficient for the series in the range  $\gamma = 24\text{--}29$  mJ/mol K<sup>2</sup>. The  $\chi(T)$  measurements up to  $1000$  K were fitted by local-moment Curie-Weiss behaviors which indicate a low Mn spin  $S \sim 1$ . The  $\chi$  data below  $T_N$  are analyzed using the Weiss molecular field theory for a planar noncollinear cycloidal AF structure with a composition-dependent pitch, following the previous neutron diffraction work of Venturini et al. [J. Alloys Compd. **256**, 65 (1997)]. Within this model, the fits indicate a turn angle between Mn ordered moments along the cycloid axis of  $\sim 100^\circ$  or  $\sim 145^\circ$ , either of which indicate dominant AF interactions between the Mn spins in the  $\text{Lu}_{1-x}\text{Sc}_x\text{MnSi}$  series of compounds.

PACS numbers: 75.25.-j, 75.40.Cx, 75.50.Ee, 72.15.Eb

## I. INTRODUCTION

Competing magnetic interactions often lead to noncollinear magnetic structures,<sup>1</sup> such as occurs in triangular lattice antiferromagnets (AFs) with the famous  $120^\circ$  ordering.<sup>2</sup> Such materials are interesting in their own right but a noncollinear magnetic structure can also occur in conjunction with other ordered states such as in magnetoelectric multiferroics. In one class of magnetoelectrics, the coupling between the electric and magnetic degrees of freedom requires a noncollinear AF spin structure.<sup>3</sup> The noncollinear magnetic structures of such materials are usually determined using neutron diffraction measurements.

One of us (DCJ) recently formulated a molecular field theory (MFT) of the anisotropic magnetic susceptibility  $\chi$  below the Néel temperature  $T_N$  of single-crystal planar noncollinear Heisenberg AFs containing identical crystallographically-equivalent spins.<sup>4</sup> This MFT allows details of the magnetic structure as well as of the magnetic interactions to be estimated from a fit to the  $\chi$  versus temperature  $T$  data in the AF state at  $T < T_N$ . The predictions are useful because they are generic, complementary to neutron diffraction measurements, and are applicable to a variety of noncollinear AF structures and materials. MFT does not account for quantum fluctuations, so it is expected to be most accurate for three-dimensional spin lattices with large spin  $S$ . On the other hand, deviations of experimental  $\chi(T < T_N)$  data from the theory can be used as a diagnostic for spin fluctuations and correlations beyond MFT, as already illustrated by fits to the anisotropic  $\chi(T < T_N)$  for single crystals of several materials.<sup>4</sup> The MFT also makes the remarkable prediction that the  $120^\circ$  triangular lattice AF

should have an *isotropic and  $T$ - and  $S$ -independent*  $\chi$  at  $T < T_N$ , as has actually been observed for many such antiferromagnets.<sup>2,4</sup> Although the MFT was formulated to fit the anisotropic  $\chi(T)$  of single crystals, it is used in this paper to model  $\chi(T \leq T_N)$  data for polycrystalline samples by taking the powder average of the single-crystal predictions.

The above MFT has mostly been applied to fitting the anisotropic  $\chi(T)$  for single-crystal AF insulators,<sup>4</sup> with the exception of a polycrystalline sample of the stoichiometric metallic compound  $\text{Y}_3\text{MnAu}_5$ , where a helical AF structure with a turn angle of  $69^\circ$  was predicted from the fit to  $\chi(T \leq T_N)$ .<sup>5</sup> A figure showing an example of a helical structure is shown in Fig. 1 of Ref. 4, which consists of ferromagnetically-aligned layers of spins in the  $xy$  plane, with the ordered moments aligned within the layer, where the direction of the ordered moments rotates by a fixed angle between  $0$  and  $180^\circ$  from layer to layer along the helix ( $z$ ) axis, so the ends of the ordered moment vectors in moving from layer to layer trace out the ridges of a screw.<sup>6</sup> The related cycloidal AF structure, illustrated here in Fig. 1, contains ordered moments also aligned in the  $xy$  plane, but where the layers of ferromagnetically aligned moments are perpendicular to the  $xy$  plane instead of being in the  $xy$  plane, and where the cycloid  $z$  axis is in the  $xy$  plane instead of perpendicular to it. In this case, the tips of the ordered moment vectors trace out a cycloid in the  $xy$  plane along the axis of the cycloid, hence the name.<sup>6</sup> The predictions of the anisotropic  $\chi(T)$  from our MFT for helical and cycloidal AF structures are identical.

The main goal of the present work is to apply the above MFT to fit  $\chi(T < T_N)$  for polycrystalline samples of the metallic  $\text{Lu}_{1-x}\text{Sc}_x\text{MnSi}$  system which crystallizes in the

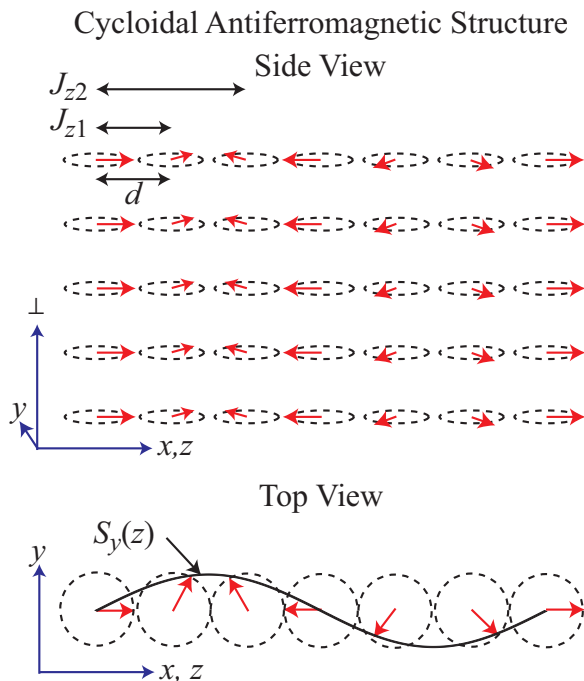


FIG. 1: (Color online) Schematic illustration of a cycloidal antiferromagnetic structure, where the wave vector  $\mathbf{k}$  of the cycloid in the  $z$ -direction is in the  $xy$ -plane in which the ordered magnetic moments reside. The “ $\perp$ ” direction is defined by  $\hat{\mathbf{i}} \times \hat{\mathbf{j}} = \hat{\mathbf{z}}$ . Vertical layers of ferromagnetically-aligned spins, separated by a distance  $d$  along the horizontal cycloid  $z$  axis, rotate their directions along this axis. The turn angle between the magnetic moments in successive layers is  $\phi_{ji} = kd = \pi/3$  in this example, which is commensurate with the spin lattice with a period  $\lambda = 2\pi/|k_z| = 6d$ . The tips of the spin or magnetic moment vectors trace out a cycloid in moving from layer to layer along the  $z$  axis, like a point on the radius of a rolling tire does. The interplanar exchange interactions  $J_{z1}$  and  $J_{z2}$  in the generic  $J_0$ - $J_{z1}$ - $J_{z2}$  model for a cycloid are indicated.

orthorhombic TiNiSi-type structure.<sup>7,8</sup> Neutron diffraction measurements by Venturini et al. indicated that this system exhibits a cycloidal AF ground state,<sup>7</sup> where the magnitude of the pitch of the cycloid depends on the Sc concentration. For  $x = 0.9$ , they found that the Mn ordered moments are aligned within the orthorhombic  $ac$  plane and the cycloid axis is the  $a$  axis; a similar AF structure is obtained for LuMnSi.<sup>7</sup> Since our MFT predicts that  $\chi(T < T_N)$  is sensitive to the pitch of a helical or cycloidal AF structure,<sup>4</sup> this system is attractive for applying the MFT predictions.

Here we present x-ray diffraction (XRD), magnetization  $M$  versus applied magnetic field  $H$ ,  $\chi(T)$ , heat capacity  $C_p(T)$  and electrical resistivity  $\rho(T)$  measurements on polycrystalline samples of  $\text{Lu}_{1-x}\text{Sc}_x\text{MnSi}$  with compositions  $x = 0, 0.25$  and  $0.5$ . Although some of our data suggest that  $\text{Lu}_{1-x}\text{Sc}_x\text{MnSi}$  may be an itinerant AF, itinerant AFs can often be parameterized by a local-moment Heisenberg model as was done for iron-arsenide high- $T_c$  superconductors and parent compounds.<sup>9</sup>

We present the experimental details in Section II and our crystallography study is described in Sec. III. The  $M(H)$  and  $\chi(T)$ ,  $C_p(T)$ , and  $\rho(T)$  measurements are presented and analyzed in Secs. IV–VI, respectively, followed by a summary in Sec. VII.

## II. EXPERIMENTAL DETAILS

Polycrystalline samples of  $\text{Lu}_{1-x}\text{Sc}_x\text{MnSi}$  ( $x = 0, 0.25$ , and  $0.5$ ) were prepared by arc-melting the high purity elements Lu from Ames Laboratory, Mn (99.99%) from Alfa Aesar and Si (99.999995%) from ROC/RIC under ultra high purity argon. The samples were turned over and remelted several times to ensure homogeneity. Fifteen wt% extra Mn was included in the starting composition to account for mass loss during arc-melting. The arc-melted samples were then annealed at 800 °C for one week. As evident in the powder XRD patterns presented in Fig. 2 below, the samples are nearly single phase. We attempted to prepare samples with higher doping levels than  $x = 0.5$ , but these samples were two-phase with large amounts of ScMnSi which forms with a different structure. In addition, unsuccessful attempts to grow single crystals with the correct phase were attempted from solution using Sn, Al, Cu, and Ga as fluxes.

Powder XRD patterns for LuMnSi were obtained with a Stoe Stadi P diffractometer employing a rotating sample holder thus alleviating preferred orientation effects that were detected with a stationary sample holder. For Sc compositions  $x = 0.25$  and  $0.5$  the powder XRD patterns were obtained with a Rigaku Giegerflex powder diffractometer using a stationary sample holder. Both diffractometers used Cu  $K_\alpha$  radiation. The crystal structures were determined by Rietveld profile analyses with the FullProf package.<sup>10</sup>

The  $M(H, T)$  and  $\chi(T)$  measurements from 1.8 to 300 K were carried out using a Quantum Design, Inc., magnetic properties measurement system (MPMS). A gelatin capsule was used as a sample holder in these measurements. For high-temperature magnetization measurements up to 1000 K, the vibrating sample magnetometer (VSM) option of the Quantum Design, Inc., physical properties measurement system (PPMS) was used. In all magnetic measurements, the sample holder was measured separately and corrected for in the data presented here. The  $C_p(T)$  measurements were done using a Quantum Design PPMS. The samples had masses of 10–15 mg and were thermally anchored to the heat capacity addenda using Apiezon N grease.

The  $\rho(T)$  was measured using the ac transport option of the PPMS. These measurements utilized rectangular-shaped samples that were cut from the arc-melted buttons using a low-speed diamond wheel saw. Platinum electrical leads were attached to the samples using silver epoxy. These measurements were performed on both cooling and heating to check for thermal hysteresis; however, no hysteresis was detected for any of the samples,

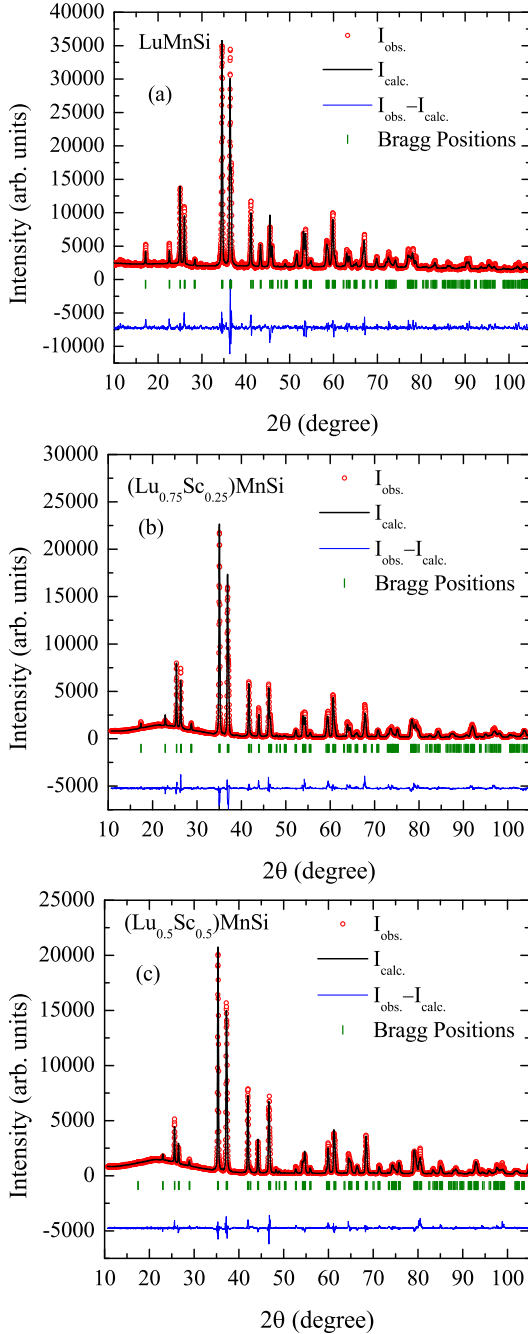


FIG. 2: (Color online) Room-temperature powder XRD patterns of (a) LuMnSi, (b) Lu<sub>0.75</sub>Sc<sub>0.25</sub>MnSi and (c) Lu<sub>0.5</sub>Sc<sub>0.5</sub>MnSi. The data are shown as open red circles, the Rietveld refinement fits as the black lines, the calculated Bragg peak positions as the vertical green tick marks, and the fit deviations at the bottom as blue lines.

indicating that the magnetic transitions in the samples are thermodynamically of second order, consistent with the results of the  $C_p(T)$  measurements. Due to uncertainties in the geometric factor, the magnitude of the  $\rho$  data have a systematic error of order 10%.

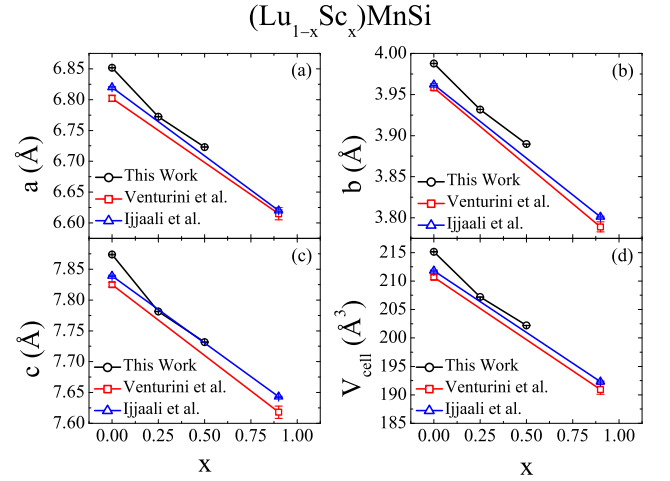


FIG. 3: (Color online) Lattice parameters (a)  $a$ , (b)  $b$  and (c)  $c$  versus composition  $x$  in Lu<sub>1-x</sub>Sc<sub>x</sub>MnSi. Panel (d) shows the unit cell volume  $V_{\text{cell}}$  versus  $x$ . Also plotted for comparison are corresponding data from Venturini et al.<sup>7</sup> and Ijjaali et al.<sup>8</sup> All lines are guides to the eye.

### III. CRYSTALLOGRAPHY

The room-temperature powder XRD patterns for Lu<sub>1-x</sub>Sc<sub>x</sub>MnSi ( $x = 0, 0.25$ , and  $0.5$ ) are shown in Fig. 2. The crystal data for the primitive orthorhombic TiNiSi-type structure (space group  $Pnma$ ) reported in Refs. 7 and 8 were used as the starting point for the Rietveld refinements. Our results confirm this structure for our samples. The refinements are shown in Fig. 2. Figure 3 shows the dependence of the lattice parameters on composition. An approximately linear decrease is observed in the  $a$ ,  $b$ , and  $c$  lattice parameters versus Sc concentration  $x$ . Table I contains listings of the lattice parameters and qualities of fit and Table II reports the atomic positions and interatomic distances that may be relevant to the magnetic structure. Our crystal data are in satisfactory agreement with those reported previously,<sup>7,8</sup> which are also listed in the two tables for comparison.

The structure of the Lu<sub>1-x</sub>Sc<sub>x</sub>MnSi system is shown in Fig. 4. The shortest interatomic distances (“bonds”) that are likely most important in determining the magnetic properties are shown, and are more clearly highlighted in Fig. 5. These figures show that the Mn atoms are arranged in distinct {Mn1,Mn3} and {Mn2,Mn4} zigzag chains running along the orthorhombic  $b$  axis with the intrachain bonds shown in black, where the designations Mn1, Mn2, Mn3 and Mn4 for the crystallographically equivalent Mn atoms are taken from Ref. 7. These zigzag chains of Mn spins were proposed in Ref. 7 to interact through superexchange interactions via the Si atoms which are denoted by gray lines in Fig. 5. The lengths of these bonds are listed in Table II. However, if the magnetism arises from local Mn magnetic moments as assumed in Ref. 7, undoubtedly RKKY interactions between the Mn spins are important in this metallic system.

TABLE I: Crystallographic properties of the  $(\text{Lu}_{1-x}\text{Sc}_x)\text{MnSi}$  system at room temperature (primitive orthorhombic  $\text{TiNiSi}$ -type structure: space group  $Pnma$ ). Listed for each composition  $x$  are the unit cell dimensions  $a$ ,  $b$ , and  $c$ ; unit cell volume  $V_{\text{cell}}$ ; and the Rietveld quality-of-fit parameters  $R_p$ ,  $R_{\text{wp}}$ , and  $\chi^2$ .

$x$	$a$ (Å)	$b$ (Å)	$c$ (Å)	$V_{\text{cell}}$ (Å <sup>3</sup> )	$R_p$	$R_{\text{wp}}$	$\chi^2$	Ref.
0	6.8519(4)	3.9877(2)	7.8737(4)	212.14(2)	6.63	8.94	19.2	This work
	6.820(1)	3.962(1)	7.839(1)	211.8(1)				8
	6.802(5)	3.958(3)	7.825(4)	210.7(5)				7
0.25	6.7724(3)	3.9318(2)	7.7813(3)	207.20(3)	8.31	11.4	10.1	This work
0.5	6.7232(3)	3.8898(2)	7.7317(3)	202.20(3)	6.77	9.75	7.11	This work
0.9	6.620(1)	3.801(1)	7.643(1)	192.29(5)				8
	6.615(10)	3.789(6)	7.618(10)	190.9(9)				7

TABLE II: Atomic coordinates of the  $(\text{Lu}_{1-x}\text{Sc}_x)\text{MnSi}$  system at room temperature. The system crystallizes in space group  $Pnma$  with  $Z = 4$  formula units per unit cell. All atoms occupy  $4c$  positions with atomic coordinates Lu:  $(x_{\text{Lu/Sc}}, 1/4, z_{\text{Lu/Sc}})$ , Mn:  $(x_{\text{Mn}}, 1/4, z_{\text{Mn}})$ , and Si:  $(x_{\text{Si}}, 1/4, z_{\text{Si}})$ . Also listed are the interatomic distances (in Å) that may be relevant to the magnetic ordering of the system. A listed Mn-Si-Mn distance is the sum of the respective Mn to Si and Si to Mn distances.

$x$	$x_{\text{Lu/Sc}}$	$z_{\text{Lu/Sc}}$	$x_{\text{Mn}}$	$z_{\text{Mn}}$	$x_{\text{Si}}$	$z_{\text{Si}}$	$d_{\text{Mn}_2-\text{Mn}_4}$	$d_{\text{Mn}_1-\text{Si}_1-\text{Mn}_2}$	$d_{\text{Mn}_1-\text{Si}_1-\text{Mn}_4}$	Ref.
0	0.0254(3)	0.6776(3)	0.1341(8)	0.0561(7)	0.275(2)	0.371(2)	2.85(1)	5.21(3)	5.19(3)	This work
	0.02488(9)	0.67835(8)	0.1378(3)	0.0572(3)	0.2742(6)	0.3765(6)	2.874(3)	5.18(2)	5.20(2)	8
	0.034(3)	0.674(3)	0.159(8)	0.052(5)	0.283(6)	0.385(5)	3.0(1)	5.1(2)	5.3(3)	7
0.25	0.0251(2)	0.6791(3)	0.1335(5)	0.0565(5)	0.280(1)	0.3691(8)	2.812(7)	5.14(3)	5.09(3)	This work
0.5	0.0258(2)	0.6808(3)	0.1388(5)	0.0627(4)	0.2708(9)	0.3750(6)	2.864(6)	5.07(2)	5.09(3)	This work
0.9	0.0281(1)	0.6756(1)	0.1378(2)	0.0560(1)	0.2696(3)	0.3711(3)	2.770(2)	5.008(8)	5.06(2)	8
	0.027(2)	0.668(2)	0.133(9)	0.051(5)	0.262(9)	0.368(6)	2.7(2)	5.0(3)	5.1(3)	7

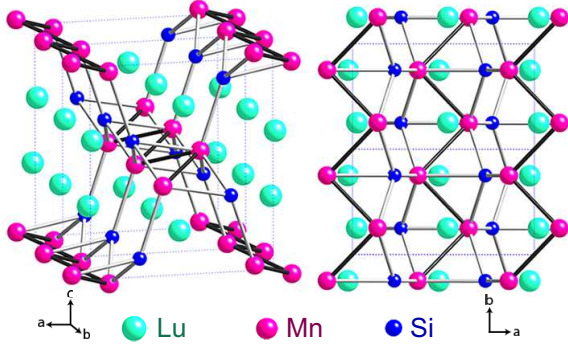


FIG. 4: (Color online) The structure of  $\text{LuMnSi}$  viewed from two different perspectives. Two unit cells are shown in each panel with the edges denoted by the thin blue dotted lines. The dark bonds are intrachain Mn-Mn bonds and the lighter ones are interchain Mn-Si-Mn bonds. The Mn zigzag chains are evident in each panel.

#### IV. ELECTRICAL RESISTIVITY

The  $\rho(T)$  data of our polycrystalline samples of  $\text{Lu}_{1-x}\text{Sc}_x\text{MnSi}$  ( $x = 0, 0.25, 0.5$ ) are presented in Fig. 6(a). The positive slopes and the magnitudes of  $\rho(T)$  indicate that the samples are metallic. Each data set shows a distinct maximum in slope at a temperature  $T_N$  as marked by the vertical arrows, which we determine below to be the AF transition temperature. This increase in slope below  $T_N$  is likely caused by the loss of

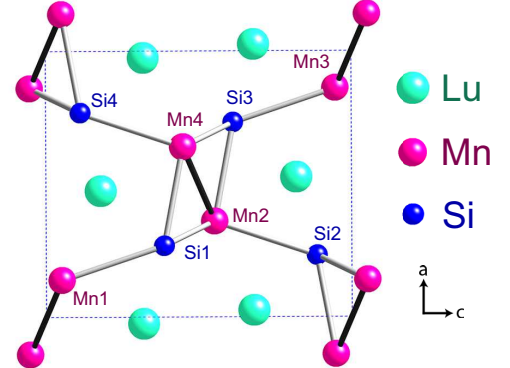


FIG. 5: (Color online) View of the  $\text{LuMnSi}$  crystal structure showing the important interactions between the Mn atoms. The black lines are the direct Mn-Mn interactions and the gray lines are the indirect Mn-Si-Mn interactions. The designations Mn1, Mn2, Mn3, Mn4, Si1, Si2, Si3 and Si4 are taken from Ref. 7. The Mn1 and Mn3 atoms and the Mn2 and Mn4 atoms respectively form distinct Mn zigzag chains running along the  $b$  axis.

spin-disorder scattering as the ordered moments in the samples increase with decreasing  $T$ . To more directly compare the  $T$  dependences of  $\rho$ , the data are normalized by  $\rho(300 \text{ K})$  and replotted in Fig 6(b).

In order to accurately determine  $T_N$  from the  $\rho(T)$  data, the temperature derivatives of the normalized data in Fig 6(b) are shown in Fig. 6(c), where a sliding least squares fit over a small temperature window was used to



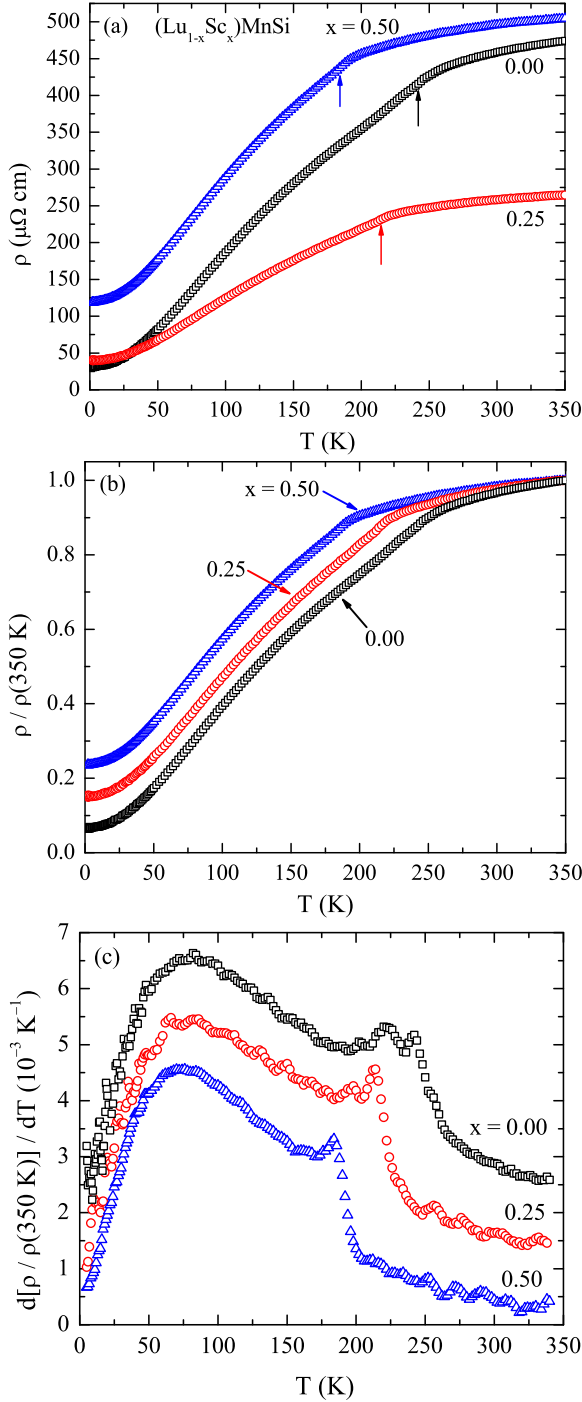


FIG. 6: (Color online) (a) Electrical resistivity  $\rho$  versus temperature  $T$  for the  $\text{Lu}_{1-x}\text{Sc}_x\text{MnSi}$  system. The vertical arrows indicate  $T_N$  as determined from the highest  $T$  peak of  $d\rho/dT$  in (c). (b)  $\rho(T)/\rho(350\text{ K})$  versus  $T$ . (c) Temperature derivative of  $\rho/\rho(350\text{ K})$   $\{d[\rho/\rho(350\text{ K})]/dT\}$  to emphasize the change in slope at  $T_N$ , which corresponds to the highest-temperature peak for each sample. Only the data above  $T = 5\text{ K}$  are plotted. For clarity, the data sets  $x = 0$  and  $0.25$  are offset vertically by  $2$  and  $1 \times 10^{-3}\text{ K}^{-1}$ , respectively. The origin of the second peak below  $T_N$  for each of the  $x = 0$  and  $0.25$  samples is not clear.

calculate the derivative at each  $T$ . Two peaks are observed in Fig. 6(c) near  $T_N$  for  $x = 0$  and  $0.25$ . The higher- $T$  peak is determined from other measurements below to be  $T_N$  as indicated by the vertical arrows in Fig 6(a). The origin of the lower- $T$  peak for each of the  $x = 0$  and  $0.25$  samples is not clear. The values of  $T_N$  thus determined for compositions  $x = 0, 0.25$ , and  $0.5$  are  $242, 214$  and  $183\text{ K}$ , respectively. These values are in reasonable agreement with the values of  $246, 215$  and  $188\text{ K}$ , respectively, that we determined from heat capacity measurements in Sec. VI below.

## V. MAGNETIZATION AND MAGNETIC SUSCEPTIBILITY

### A. Molecular Field Theory of the Magnetic Susceptibility of a Planar Helical or Cycloidal Antiferromagnetic Structure

Before presenting the experimental  $\chi(T)$  data in the following section, we review the molecular field theory (MFT) predictions used to analyze the data.<sup>4</sup> These predictions are based on a local-moment Heisenberg model where all spins are identical and crystallographically equivalent, as occurs for the Mn spins in the  $\text{Lu}_{1-x}\text{Sc}_x\text{MnSi}$  system. The MFT that we use here for a coplanar cycloid AF structure is formulated in terms of a  $J_0$ - $J_{z1}$ - $J_{z2}$  model shown in Fig. 1, where  $J_0$  is the sum of all the interactions of a given spin with spins in the same vertical layer,  $J_{z1}$  the sum of the interactions of a given spin to all spins in a nearest-neighbor layer along the cycloid  $z$  axis, and  $J_{z2}$  the sum of the interactions of a given spin to all spins in a next-nearest neighbor layer.<sup>4</sup> The same theory applies to the helical AF structure. The direction of the in-plane ordered moments rotates by a radian angle of  $kd$  (see below) from layer to layer along the respective helix or cycloid  $z$  axis.

In the paramagnetic state at  $T \geq T_N$ , the measured  $\chi(T)$  is a  $T$ -independent orbital susceptibility  $\chi_0$  plus the spin susceptibility given by a Curie-Weiss law, i.e.,

$$\chi(T) = \chi_0 + \frac{C}{T - \theta_p}, \quad (1)$$

where  $\chi_0$  can be anisotropic and generally consists of the diamagnetic core, anisotropic paramagnetic Van Vleck, and conduction carrier Landau diamagnetic susceptibilities. Also,  $\theta_p$  is the Weiss temperature, the Curie constant  $C$  is

$$C = \frac{Ng^2S(S+1)\mu_B^2}{3k_B}, \quad (2)$$

$N$  is the number of spins,  $g$  is the spectroscopic splitting factor ( $g$ -factor),  $\mu_B$  is the Bohr magneton and  $k_B$  is Boltzmann's constant. For the helical or cycloidal AF structure, using MFT one can write  $\theta_p$  and  $T_N$  in terms

of the above-defined  $J_0$ ,  $J_{z1}$ ,  $J_{z2}$  interactions as<sup>4</sup>

$$k_B\theta_p = -\frac{S(S+1)}{3}(J_0 + 2J_{z1} + 2J_{z2}), \quad (3a)$$

$$k_B T_N = -\frac{S(S+1)}{3} \times [J_0 + 2J_{z1} \cos(kd) + 2J_{z2} \cos(2kd)], \quad (3b)$$

where  $k$  is the magnitude of the helix or cycloid wave vector,  $d$  is the distance between adjacent ferromagnetically-aligned layers of spins, and therefore  $kd$  is the turn angle in radians along the  $z$ -axis between spins in adjacent spin layers. After writing the classical energy of the helix or cycloid at  $T = 0$  in terms of the above exchange constants and  $kd$ , minimizing the energy with respect to  $kd$  yields the relationship

$$\cos(kd) = -\frac{J_{z1}}{4J_{z2}}. \quad (3c)$$

In general,  $\theta_p$  and  $T_N$  in Eqs. (3a) and (3b), respectively, are known from the experimental  $\chi(T)$  data and  $S$  can be estimated from these data or other considerations. The value of  $kd$  in Eq. (3c) can be obtained from the experimental value of  $\bar{\chi}_{xy}(T = 0)$  using Eq. (5g) below. Then the values of  $J_0$ ,  $J_{z1}$ ,  $J_{z2}$  are obtained by solving the three simultaneous Eqs. (3) using the known values of  $\theta_p$ ,  $T_N$ ,  $S$  and  $kd$ .

When  $H$  is applied perpendicular to the ordering plane of any collinear or planar noncollinear AFM structure containing identical crystallographically equivalent spins interacting by Heisenberg exchange, MFT predicts that the perpendicular magnetic susceptibility  $\chi_\perp$  at  $T \leq T_N$  is constant and equal to the value at  $T_N$ ,<sup>4</sup> i.e., the dimensionless reduced perpendicular susceptibility  $\bar{\chi}_\perp(T)$  is

$$\bar{\chi}_\perp(T \leq T_N) \equiv \frac{\chi_\perp(T \leq T_N)}{\chi(T_N)} = 1. \quad (4)$$

When  $H$  is applied in the plane of the spins of a planar ( $xy$ ) noncollinear AF structure, MFT predicts that the dimensionless reduced susceptibility is<sup>4</sup>

$$\bar{\chi}_{xy}(t) \equiv \frac{\chi_{xy}(T)}{\chi(T_N)} = \frac{(1 + \tau^* + 2f + 4B^*)(1 - f)}{2[(\tau^* + B^*)(1 + B^*) - (f + B^*)^2]}, \quad (5a)$$

where the dimensionless reduced variables are

$$\tau^* = \frac{(S+1)t}{3B'_S(y_0)}, \quad y_0 = \frac{3\bar{\mu}_0}{(S+1)t}, \quad (5b)$$

$$B^* = 2(1 - f) \cos(kd)[1 + \cos(kd)] - f, \quad (5c)$$

$$f = \frac{\theta_p}{T_N}, \quad (5d)$$

$$t = \frac{T}{T_N}. \quad (5e)$$

The reduced ordered moment in applied field  $H = 0$  is defined as  $\bar{\mu}_0(t) \equiv \mu_0(t)/\mu_0(0)$ , where  $\mu_0(t)$  is the

temperature-dependent ordered moment below  $T_N$ . The value of  $\bar{\mu}_0$  is obtained by numerically solving

$$\bar{\mu}_0 = B_S(y_0), \quad (5f)$$

and the value of  $f$  is usually uniquely defined from the measured values of  $\theta_p$  and  $T_N$ . The sign of  $f$  is the same as the sign of  $\theta_p$  and can therefore be either positive or negative.

The expression for  $B^*$  in Eq. (5c) applies specifically to a planar cycloid with the cycloid axis being the  $z$  axis which is parallel to the  $xy$  plane in which the ordered moments are aligned for  $T < T_N$  (see Fig. 1). At  $T = 0$ , Eq. (5a) yields

$$\bar{\chi}_{xy}(T = 0) = \frac{1}{2[1 + 2\cos(kd) + 2\cos^2(kd)]}, \quad (5g)$$

which does not contain the parameter  $f$ . However, the temperature dependence of  $\bar{\chi}_{xy}$  does depend on  $f$  according to Eq. (5a). Our unconventional definition of the Brillouin function and its derivative are

$$B_S(y_0) = \frac{1}{2S} \left\{ (2S+1) \coth \left[ (2S+1) \frac{y_0}{2} \right] - \coth \left[ \frac{y_0}{2} \right] \right\},$$

$$B'_S(y_0) = \frac{1}{4S} \left\{ \operatorname{csch}^2 \left( \frac{y_0}{2} \right) - (2S+1)^2 \operatorname{csch}^2 \left[ (2S+1) \frac{y_0}{2} \right] \right\}. \quad (5h)$$

For a polycrystalline sample, one measures the powder-averaged susceptibility  $\chi_P$  given in reduced units using Eq. (4) as

$$\bar{\chi}_P(T) \equiv \frac{\chi_P(T)}{\chi(T_N)} = \frac{1}{3} [\bar{\chi}_\perp + 2\bar{\chi}_{xy}(T)] = \frac{1}{3} [1 + 2\bar{\chi}_{xy}(T)]. \quad (6a)$$

Then using Eqs. (5g) and (6a), in the ordered cycloidal AF state at  $T = 0$  one obtains

$$\bar{\chi}_P(T = 0) = \frac{1}{3} \left[ 1 + \frac{1}{1 + 2\cos(kd) + 2\cos^2(kd)} \right], \quad (6b)$$

which allows the cycloid turn angle  $kd$  to be determined from the measured values of  $\chi_P(T = 0)$  and  $\chi(T_N)$ . A plot of  $\bar{\chi}_P(T = 0)$  versus  $kd$  according to Eq. (6b) is shown in Fig. 7. A turn angle  $kd$  less than  $\pi/2$  rad indicates that the dominant interactions in the system are ferromagnetic, since in this case there is a component of the ordered moments in adjacent layers that are in the same direction. Conversely, a turn angle  $kd$  greater than  $\pi/2$  rad indicates that the dominant interactions in the system are antiferromagnetic.

Figure 7 shows that for  $2/3 < \bar{\chi}_P(T = 0) < 1$  as found below for the  $\text{Lu}_{1-x}\text{Sc}_x\text{MnSi}$  system, the derived value of  $kd$  is not unique since for a  $\bar{\chi}_P(T = 0)$  value in this range Eq. (6b) yields two possible values of  $kd$  with  $\pi/2 < kd < \pi$ . A corresponding plot of  $\bar{\chi}_{xy}(T = 0)$  versus  $kd$  from Eq. (5g) that can be used to analyze single-crystal  $\bar{\chi}_{xy}(T = 0)$  data is shown in Fig. 2(a) of Ref. 4.

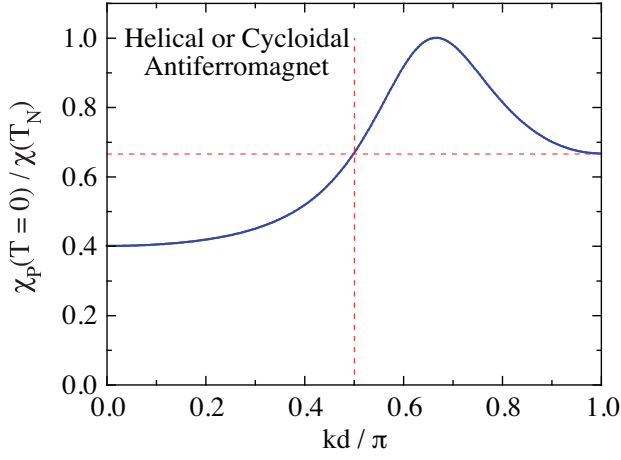


FIG. 7: (Color online) Reduced powder susceptibility  $\bar{\chi}_P(T=0) \equiv \chi_P(T=0)/\chi(T_N)$  versus the turn angle  $kd$  in radians for a helical or cycloidal Heisenberg antiferromagnet according to Eq. (6b) (solid blue curve). For the upper right quadrant with  $\pi/2 < kd < \pi$  defined by the red dashed horizontal and vertical lines, there are two possible values of  $kd$  for a given value of  $\bar{\chi}_P(T=0)$ . The special point at the maximum of the curve with  $kd = 2\pi/3$  and  $\bar{\chi}_P(T=0) = 1$  corresponds to  $120^\circ$  ordering of a triangular lattice antiferromagnet for which the single-crystal  $\chi$  is isotropic and independent of  $T$  and spin  $S$  below  $T_N$ ,<sup>4</sup> and hence the powder average is also independent of  $T$  and  $S$  below  $T_N$ .

### B. Magnetization and Magnetic Susceptibility Measurements and Analysis

$M(H)$  isotherms were measured for each of the three  $\text{Lu}_{1-x}\text{Sc}_x\text{MnSi}$  ( $x = 0, 0.25, 0.5$ ) samples in magnetic fields up to  $H = 5.5$  T at eight temperatures between 1.8 and 300 K as shown in Fig. 8. The data show that  $M$  is proportional to  $H$  over the entire field range for each of the samples, thus indicating that ferromagnetic or saturable paramagnetic impurities are not detected in this temperature range for any of the samples.

The  $\chi(T) \equiv M(T)/H$  measurements for 1.8 to 1000 K carried out at various  $H$  are shown in Fig. 9(a) and the data below 350 K are shown separately in Fig. 10. The inverse susceptibility  $\chi^{-1}$  is plotted versus  $T$  in Fig. 9(b). In Figs. 9(a), 9(b) and 10(a), our data for the  $x = 0$  sample are compared with the results of a previous study for the same composition.<sup>7</sup> For  $T < T_N$ , good agreement is observed between these data sets. However the data in the paramagnetic region at  $T > T_N$  differ significantly. This resulted in different values for  $C$  and  $\theta_p$  from Curie-Weiss fits to the two respective data sets.

The  $\chi^{-1}(T)$  data in Fig. 9(b) were fitted by the inverse of the expression for the susceptibility in Eq. (1). In the sample with composition  $x = 0.25$ , a break in slope is observed at  $T = 550$  K. The cause of this feature is unknown and Eq. (1) was fitted to the data above this temperature. The  $T$  range of the fits and the pa-

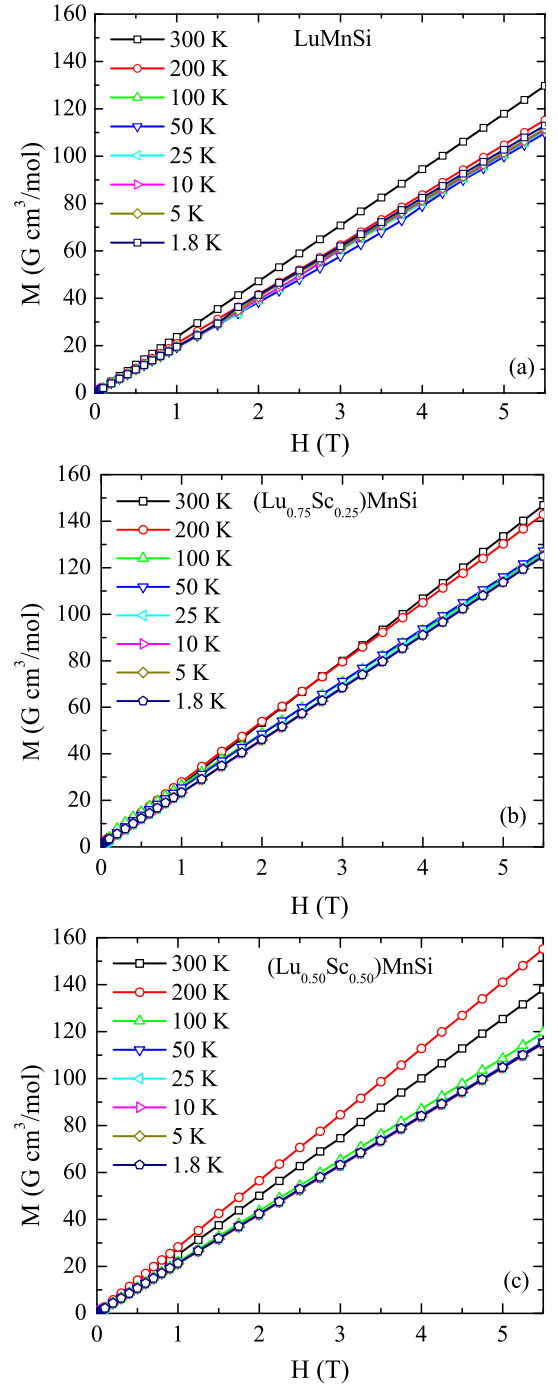


FIG. 8: (Color online) Magnetization  $M$  versus applied magnetic field  $H$  isotherms for samples in the  $\text{Lu}_{1-x}\text{Sc}_x\text{MnSi}$  system for compositions (a)  $x = 0$  (b)  $x = 0.25$ , and (c)  $x = 0.5$ . The lines connecting the data points are guides to the eye.

rameters obtained are given in Table III. The parameter  $f = \theta_p/T_N$  in Eq. (5d) is calculated from the resulting value of  $\theta_p$  and the  $T_N$  determined from heat capacity measurements below.

The values of the Curie constant per mole of Mn,  $C_{\text{Mn}}$ , for the  $x = 0$  and 0.5 samples are 1.26 and



TABLE III: Parameters obtained by fitting the high-temperature  $\chi^{-1}$  versus  $T$  data and low-temperature ( $T < T_N$ )  $\chi/\chi(T_N)$  versus  $T/T_N$  data in Fig. 11. Listed are the  $T$  range used to fit the high-temperature  $\chi^{-1}$  data in Fig. 9(b),  $T_N$  as determined from the peak in  $d(\chi T)/dT$ , Weiss temperature  $\theta_p$ , the calculated ratio  $f \equiv \theta_p/T_N$ , Curie constant  $C_{Mn}$  per mole of Mn atoms, effective moment  $\mu_{\text{eff}}(\mu_B/\text{Mn}) = \sqrt{8C_{Mn}}$ ,  $T$ -independent contribution  $\chi_0$  to  $\chi$ , and cycloid turn angle  $kd$  for the different compositions  $x$ . Two values of  $kd$  are listed for reasons described in the text. Also included are literature data from Ref. 7.

$x$	$T$ range (K)	$T_N$ (K)	$\theta_p$ (K)	$f$	$C_{Mn}$ ( $\frac{\text{cm}^3 \text{K}}{\text{mol Mn}}$ )	$\mu_{\text{eff}}$ ( $\mu_B/\text{Mn}$ )	$\chi_0$ ( $\frac{10^{-3} \text{cm}^3}{\text{mol}}$ )	$kd$ (deg)	Ref.
0	350–1000	246	−352(2)	−1.43	1.262(5)	3.18	0.544(3)	104 or 139	This work
0		255	−201		1.25	3.17			7
0.25	550–1000	215	114(2)	0.531	0.551(3)	2.10	0.781(2)	98.9 or 147	This work
0.5	300–1000	189	−125.2(8)	−0.662	0.789(2)	2.51	0.659(2)	96.5 or 153	This work
0.9		125	166		0.374	1.73			7

0.79 cm<sup>3</sup> K/mol Mn, respectively. Curie constants  $C_{Mn} = 0.375$ , 1 and 1.875 cm<sup>3</sup> K/mol Mn correspond to Mn spins  $S = 1/2$ , 1 and  $3/2$  with  $g = 2$  in a local moment picture, respectively, indicating that within this picture the Mn spins are rather small compared to the value  $S = 5/2$  for a high-spin Mn<sup>2+</sup> local moment with  $C_{Mn} = 4.38$  cm<sup>3</sup> K/mol Mn and  $g = 2$ . We note that Venturini et al.<sup>7</sup> found from their neutron diffraction measurements that the ordered moment of LuMnSi at 2 K is  $\mu = 2.18 \mu_B/\text{Mn}$ , which in a local moment picture corresponds to a spin  $S = \mu/(g\mu_B) = 1.08$  with  $g = 2$ , close to the value  $S = 1.16$  estimated for LuMnSi from the above value of the Curie constant for this compound with  $g = 2$ . In the analysis below of the data, we assume that the Mn spin is  $S = 1$  and  $g \approx 2$ . The variability in  $C_{Mn}$  with  $x$  suggests that Lu<sub>1-x</sub>Sc<sub>x</sub>MnSi may be an itinerant spin system. However, itinerant spin systems are often modeled using a local moment picture as carried out for the iron-arsenide high- $T_c$  superconductors.<sup>9</sup>

The slopes of the proportional  $M(H)$  data in Fig. 8 were determined by fitting the high-field data with  $H \geq 1$  T and are plotted as the filled stars in Fig. 10. We expected and found that these data are in good agreement with the respective  $\chi \equiv M/H$  data for  $H > 1$  T. The data in Fig. 10 for all three samples exhibit long-range AF order at Néel temperatures  $T_N \sim 200$ –250 K. The  $T_N$  of each sample is the temperature of the maximum of the respective derivative  $d(\chi T)/dT$  (Ref. 11) as plotted in Fig. 9(c). The  $T_N$  for each sample is reported in Table III.

In addition to the AF transition seen in  $\chi(T)$  at  $T_N$  in Fig. 10, each sample shows an anomaly at a lower  $T$  and at low fields that may reflect a change in the magnetic structure from an incommensurate cycloidal structure (see below) to a commensurate one. This anomaly is at  $\approx 140$ , 80 and 70 K for  $x = 0$ ,  $x = 0.25$  and  $x = 0.5$ , respectively. Neutron diffraction measurements specifically directed at this question are needed to resolve it. As seen in Fig. 10, the transitions at  $T_N$  are not significantly affected by fields up to 5.5 T, whereas the lower- $T$  transitions are completely suppressed by  $H = 5.5$  T.

For the purpose of analyzing  $\chi(T = 0)$  and the  $T$  dependence of  $\chi$  for  $0 < T < T_N$ , in Fig. 11 are plotted

the normalized susceptibilities  $\bar{\chi}(T) \equiv \chi(T)/\chi(T_N)$  of the two samples with  $x = 0$  and 0.5 in  $H = 5.5$  T from Fig. 10. We omit the data for the sample with  $x = 0.25$  in this figure because of the  $\chi(T)$  anomaly at  $T = 550$  K that drastically affects the value of  $f$  for this sample that is needed to analyze the temperature dependence of  $\chi$  below  $T_N$ .

Within MFT, the powder-averaged and normalized  $\bar{\chi}(T = 0)$  for a collinear local-moment Heisenberg AF is  $\bar{\chi}(T = 0) = 2/3$ , whereas Fig. 10 shows that the  $\bar{\chi}(T = 0)$  values for the three samples are in the range 0.74–0.88. This difference suggests a noncollinear ground state for each sample at  $H = 5.5$  T as discussed above. We therefore assume that the magnetic structure of the ground state is a planar noncollinear cycloid as proposed for Lu<sub>0.1</sub>Sc<sub>0.9</sub>MnSi in Ref. 7 and illustrated in our Fig. 1. As discussed in Sec. V A, the turn angle  $kd$  between successive layers of spins can be estimated from the normalized value of the powder susceptibility  $\bar{\chi}_P(T = 0)$  according to Eq. (6b) and Fig. 7. From Fig. 7, the observed values  $\bar{\chi}_P(T = 0) = 0.72$ –0.88 are in the range in which two solutions for  $kd$  are possible. The obtained values of  $kd$  are presented in Table III and plotted as a function of  $x$  in Fig. 12.

Taking the smaller of the two possible values of  $kd$  (Ref. 7) for the  $x = 0$  and 0.5 samples and the measured values of  $f$  for the two samples, the temperature dependences of  $\chi_P$  in Eq. (6a) are fully determined. These MFT predictions assume that  $S = 1$  as estimated from the above Curie-Weiss fits. The fits are compared with our observed data in Fig. 11 for  $x = 0$  and  $x = 0.5$ . Expanded plots of the data and fits are shown in the inset of Fig. 11.

The temperature dependences of our data in Fig. 11 are not described very well by the MFT. It was observed in Ref. 4 that fits of such experimental data by the MFT prediction deviate from the data as the spin quantum number decreases, and this deviation is in the same direction as seen in Fig. 11. This occurs because molecular field theory does not include the influence of quantum fluctuations arising from finite spin. Therefore, within the local-moment model the discrepancy between theory and experiment in Fig. 11 is due to the small spin  $S \sim 1$

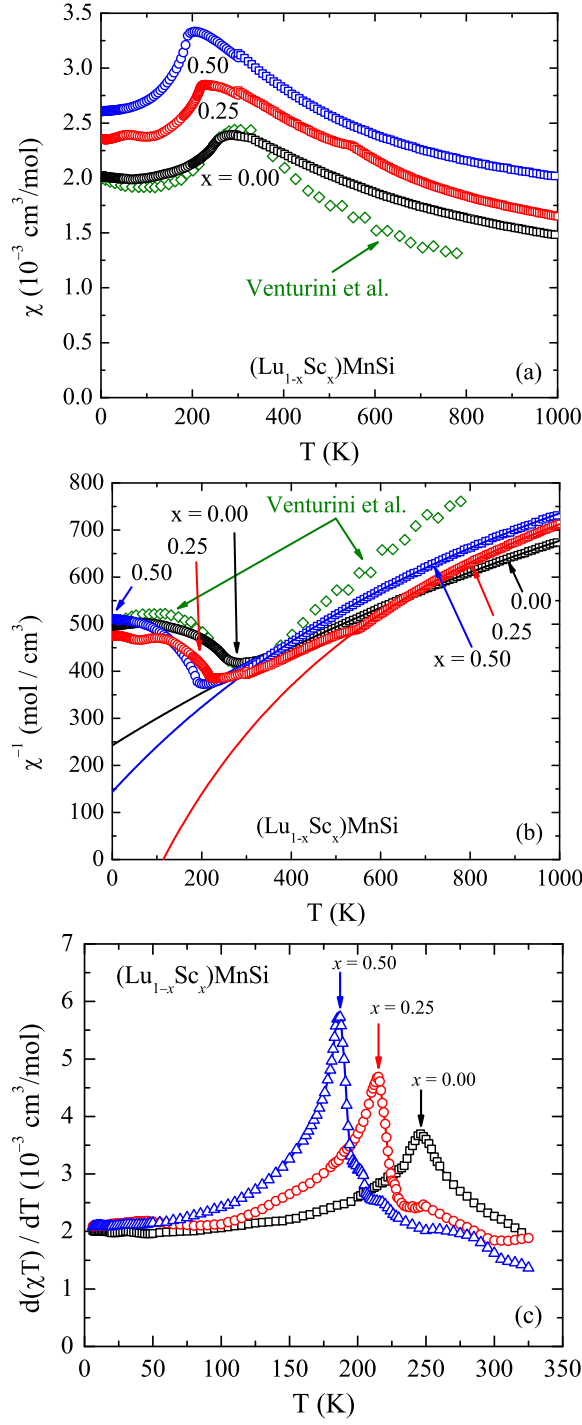


FIG. 9: (Color online) (a,b) Magnetic susceptibility  $\chi$  versus temperature  $T$  for samples in the  $\text{Lu}_{1-x}\text{Sc}_x\text{MnSi}$  system. Data below 300 K were measured on a SQUID magnetometer (MPMS, circles) and data above 300 K were measured on a VSM (squares). The SQUID data were measured in an applied field  $H = 5.5$  T and the VSM in  $H = 3.0$  T. For clarity, the data for  $x = 0.25$  and  $x = 0.50$  are offset by  $0.25 \times 10^{-3}$  and  $0.65 \times 10^{-3} \text{ cm}^3/\text{mol}$ , respectively. One data point is plotted for every five measured for the composition  $x = 0.25$  and one of every twenty measured for  $x = 0.00$  and  $0.50$ . The solid curves are fits by the modified Curie-Weiss law in Eq. (1). For comparison, also shown are the data from Ref. 7 for  $x = 0$  in  $H = 1.2$  T. (c) Plot of  $d[\chi(T)/dT]$  versus  $T$ . The numerical derivative was evaluated using a sliding-window least-squares fit.

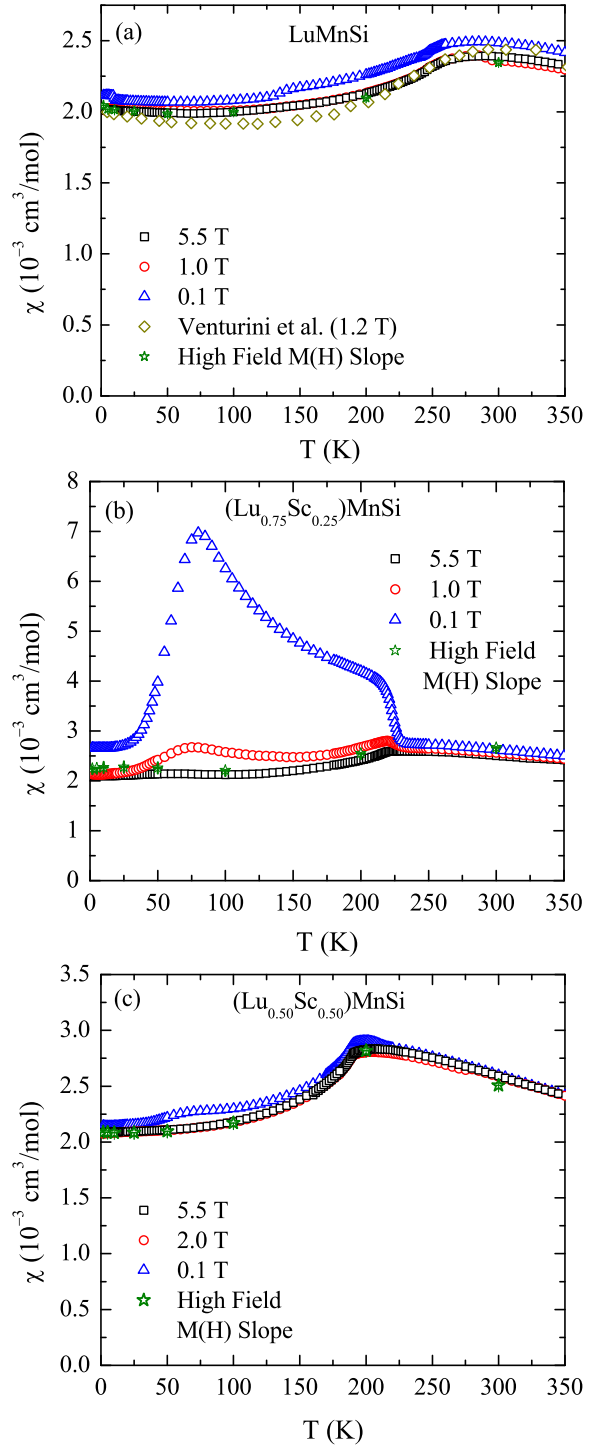


FIG. 10: (Color online) Magnetic susceptibility  $\chi \equiv M/H$  versus temperature  $T$  data for samples in the  $\text{Lu}_{1-x}\text{Sc}_x\text{MnSi}$  system with compositions (a)  $x = 0$ , (b)  $x = 0.25$ , and (c)  $x = 0.50$ . In (a) data from Ref. (7) are also plotted for comparison. The values of the high-field  $M(H)$  slopes (stars) were obtained from a linear fit of the  $M(H)$  data in Fig. 8 above  $H = 1$  T. The low- $T$  transition for each sample (possibly a spin-reorientation transition) is seen to be suppressed by  $H = 5.5$  T.

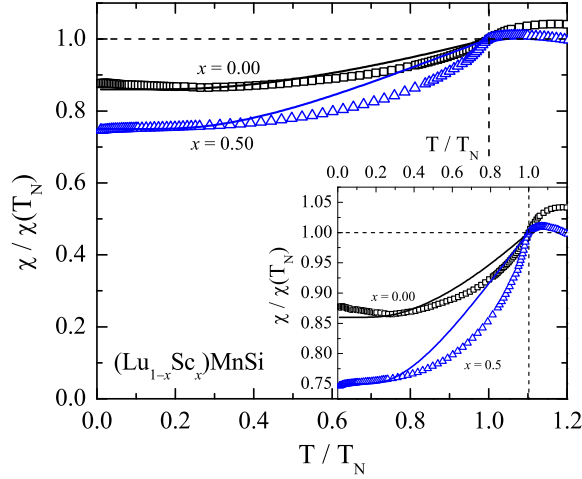


FIG. 11: (Color online) Normalized magnetic susceptibility  $\chi(T)/\chi(T_N)$  versus normalized temperature  $T/T_N$  for samples in the  $\text{Lu}_{1-x}\text{Sc}_x\text{MnSi}$  system. The solid curves are fits by MFT assuming  $S = 1$  as described in the text with parameters listed in Table III. Inset: expanded plots of the data and fits.

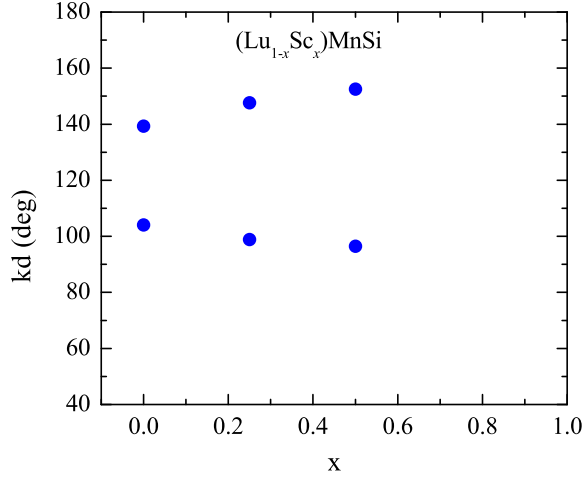


FIG. 12: (Color online) Cycloid turn angle  $kd$  versus composition  $x$  for samples in the  $\text{Lu}_{1-x}\text{Sc}_x\text{MnSi}$  system. There are two solutions of Eq. (6b) for  $kd$  for each composition as described in the text.

of the Mn atoms.

The exchange constants  $J_0$ ,  $J_{z1}$  and  $J_{z2}$  within the cycloidal model in Fig. 1 for the  $x = 0$  and  $0.5$  samples are obtained by solving the system of equations (3), where the input parameters are  $S$ ,  $\theta_p$ ,  $T_N$  and  $kd$ . The results are presented in Table IV for both of the possible values of  $kd$  for the samples with  $x = 0$  and  $0.5$  in Table IV, where we assume  $S = 1$ . For each composition, the in-plane Mn–Mn interactions are ferromagnetic (negative), consistent with the cycloidal AF model (see Fig. 1). Furthermore, for each sample the sum of the exchange interactions of a Mn spin with all other spins is  $J_0 + 2J_{z1} + 2J_{z2} > 0$ , confirming that the dominant

TABLE IV: Estimates of the exchange constants in the  $\text{Lu}_{1-x}\text{Sc}_x\text{MnSi}$  system for samples with  $x = 0$  and  $0.5$  using the assumed  $J_0$ - $J_{z1}$ - $J_{z2}$  model. These are obtained by solving the system of equations in Eqs. (3). Two solutions for  $kd$  in Eqs. (3) are given for each composition for a given value of  $\bar{\chi}_P(T = 0)$  as discussed in the text, and hence two sets of exchange constants for each composition. Values for  $x = 0.25$  are not listed due to an ambiguity caused by the different behaviors of  $\chi(T)$  for  $T > 300$  K.

$x$	$kd$ (deg)	$J_0/k_B$ (K)	$J_{z1}/k_B$ (K)	$J_{z2}/k_B$ (K)
0	104	-44(1)	140.6(5)	145.4(5)
	139	-57(2)	219.8(7)	72.8(3)
0.5	96.5	-87.3(5)	42.9(2)	94.7(3)
	153	-111.7(5)	116.9(3)	32.8(2)

TABLE V: Parameters obtained by fitting the low- $T$   $C_p/T$  versus  $T^2$  data for  $\text{Lu}_{1-x}\text{Sc}_x\text{MnSi}$  samples with  $x = 0, 0.25$  and  $0.5$  in Fig. 13(b) by Eq. (7). Listed are the electronic specific heat coefficient  $\gamma$ , the  $T^3$  coefficient  $\beta$ , lower limits to the Debye temperature  $\Theta_D$  calculated from  $\beta$  and the  $T$  range of data fitted for each composition  $x$ . The Néel temperatures  $T_N$  obtained from the heat capacity measurements are also listed.

$x$	$\gamma$ (mJ/mol K <sup>2</sup> )	$\beta$ (mJ/mol K <sup>4</sup> )	$\Theta_D$ (K)	$T$ Range (K)	$T_N$ (K)
0	24.26(7)	0.158(2)	333(2)	1.81–9.92	245.8
0.25	27.58(9)	0.125(2)	360(2)	1.81–9.68	214.6
0.5	28.73(5)	0.096(2)	393(3)	1.82–8.20	187.7

Mn–Mn interactions in the system are antiferromagnetic as discussed above.

## VI. HEAT CAPACITY

The  $C_p$  of our three samples measured in  $H = 0$  and in the  $T$  range 1.8–300 K are presented in Fig. 13(a). A sharp peak is evident for each sample close to its  $T_N$  as determined from the above  $\chi(T)$  measurements. The  $T_N$  obtained from the  $C_p(T)$  measurements for the three compositions are listed in Table V. The noise seen in Fig. 13(a) for the samples with  $x = 0$  and  $0.25$  is believed due to instrumental effects associated with the PPMS.

In order to isolate the electronic from other contributions to the heat capacity, the low- $T$  data are plotted as  $C_p/T$  versus  $T^2$  in Fig. 13(b). We fitted these data by

$$\frac{C_p}{T} = \gamma + \beta T^2, \quad (7)$$

where  $\gamma T$  is the electronic contribution to  $C_p$ ,  $\gamma$  is the Sommerfeld electronic heat capacity coefficient and  $\beta$  is the coefficient of the  $T^3$  contribution to  $C_p$ . The  $T$  range of each fit and the fitting parameters obtained are given in Table V. It is seen that  $\gamma$  monotonically increases and  $\beta$  decreases with increased Sc concentration.

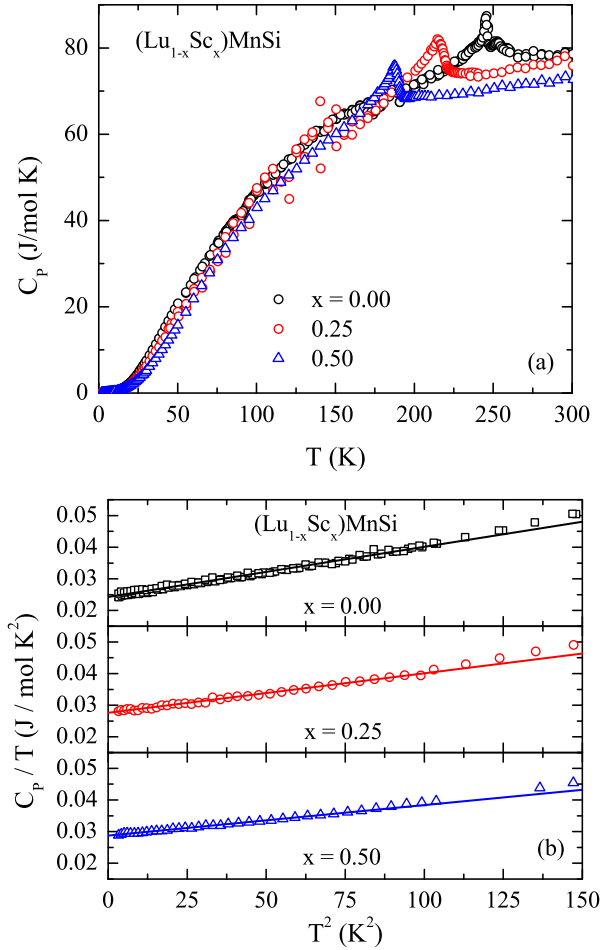


FIG. 13: (Color online) (a) Heat capacity at constant pressure  $C_p$  versus temperature  $T$  for samples in the  $\text{Lu}_{1-x}\text{Sc}_x\text{MnSi}$  system. (b) Low- $T$  plot of  $C_p/T$  versus  $T^2$  according to Eq. (7). The straight lines of corresponding color are linear fits and the fit parameters  $\gamma$  and  $\beta$  are listed in Table V. The maximum temperature of the fits is 9.9 K (see Table V), and the extensions of the lines to  $T^2 = 150 \text{ K}^2$  are extrapolations.

The  $T^3$  contribution to  $C_p$  could come from a contribution from three-dimensional AF spin waves in addition to that from the lattice. Neglecting the possible spin-wave contribution, lower limits of the Debye temperature  $\Theta_D$  are obtained from the values of  $\beta$  according to

$$\Theta_D = \left( \frac{12\pi^4 R n}{5\beta} \right)^{1/3}, \quad (8)$$

where  $n = 3$  is the number of atoms per f.u. and  $R$  is the molar gas constant. The values of  $\Theta_D$  for the three scandium concentrations are listed in Table V and are seen to increase monotonically with increasing  $x$ .

Assuming that the value of  $\gamma$  is independent of  $T$  below 300 K, one obtains the electronic heat capacity at  $T = 300 \text{ K}$  for each sample as  $C_e(300 \text{ K}) = \gamma T$  using the respective value of  $\gamma$  in Table V. The Dulong-Petit high- $T$  limit of the lattice heat capacity at constant volume

$C_{\text{latt}}$  due to acoustic lattice vibrations is  $C_{\text{latt}} = 3nR = 74.8 \text{ J/mol K}$ . The sum of  $C_e$  at 300 K and the Dulong-Petit value of  $C_{\text{latt}}$  is 82.1, 83.1 and 83.4 J/mol K for  $x = 0, 0.25$  and  $0.5$ , respectively, which are somewhat larger than the respective experimental values at 300 K in Fig. 13(a). This is consistent with expectation, since the values of  $\Theta_D$  in Table V are all greater than 300 K and therefore  $C_{\text{latt}}$  at 300 K for each sample is significantly below its high- $T$  limit.

## VII. SUMMARY

Nearly single-phase polycrystalline samples of the  $\text{Lu}_{1-x}\text{Sc}_x\text{MnSi}$  system with compositions  $x = 0, 0.25$ , and  $0.5$  were prepared and studied. Rietveld refinements of powder XRD patterns confirmed that this system crystallizes in the primitive orthorhombic  $\text{TiNiSi}$ -type structure. The lattice parameters were found to decrease almost linearly with increasing Sc content, consistent with the smaller size of Sc relative to Lu. The Mn atoms form zigzag chains. The distance between Mn atoms in these chains is found to generally decrease as the smaller Sc atoms are substituted for the Lu atoms.

The  $\rho(T)$  data for our three samples in the  $\text{Lu}_{1-x}\text{Sc}_x\text{MnSi}$  system showed positive temperature coefficients with magnitudes in the metallic range, indicating that this system is metallic. The  $C_p(T)$ ,  $\chi(T)$ , and  $\rho(T)$  measurements indicate the occurrence of a bulk AF transition in each sample with AF ordering temperatures  $T_N = 246, 215$  and  $188 \text{ K}$  for  $x = 0, 0.25$  and  $0.5$ , respectively, where the listed  $T_N$  values were obtained from the  $C_p(T)$  measurements. A second transition is observed at lower  $T$  for each sample from the  $\chi(T)$  measurements at  $H = 0$  that is completely suppressed in  $H = 5.5 \text{ T}$ , which we speculate are due to spin reorientation transitions.

The Sommerfeld linear heat capacity coefficient  $\gamma$  and the coefficient  $\beta$  of the  $T^3$  contribution were extracted from the  $C_p$  data at  $T < 10 \text{ K}$ . The  $\gamma$  values showed enhanced values of 24.3, 27.6 and 28.7 mJ/mol K<sup>2</sup> for  $x = 0, 0.25$  and  $0.5$ , respectively, whereas the  $\beta$  values decreased significantly with increasing  $x$  with values of 0.158, 0.125 and 0.096 mJ/mol K<sup>4</sup>, respectively. The  $\beta$  values may include a significant contribution from three-dimensional AF spin waves in addition to the lattice contribution; with the information available we cannot separate these contributions.

We performed field- and temperature-dependent measurements of the magnetic properties up to 1000 K. The high- $T$   $\chi$  data are well described by Curie-Weiss behaviors with small Mn spin  $S \sim 1$ . The Curie constant was found to vary between the three compositions, which suggests that  $\text{Lu}_{1-x}\text{Sc}_x\text{MnSi}$  may be an itinerant magnetism system. However, we proceeded to analyze the  $\chi(T \leq T_N)$  data in the local moment picture as done in the past for other itinerant magnetism systems (see, e.g., Ref. 9).

The main goal of this work was to apply our re-

cent molecular field theory for  $\chi(T \leq T_N)$  of planar noncollinear AF structures of local moments interacting by Heisenberg exchange<sup>4</sup> to polycrystalline samples of the  $\text{Lu}_{1-x}\text{Sc}_x\text{MnSi}$  system. This system was reported from neutron diffraction measurements to have a planar cycloidal ground state with a composition-dependent pitch.<sup>7</sup> Analysis of our  $\chi(T \leq T_N)$  data for three compositions of  $\text{Lu}_{1-x}\text{Sc}_x\text{MnSi}$  were consistent with a composition-dependent angle between adjacent ferromagnetically-aligned Mn layers for a cycloidal AF ground state structure in the vicinity of either  $\sim 100^\circ$  or  $\sim 145^\circ$ ; from our analysis we cannot distinguish between these two possibilities. Within this model, we estimated the exchange interactions between a Mn spin and Mn spins in the same and other planes of spins along the cycloid axis. Due to ambiguities in the description of the AF structures in Ref. 7, we were not able to quantitatively compare our predictions for the rotation angles with the results in that reference.

We have shown that analyses of  $\chi(T \leq T_N)$  data for polycrystalline samples, assuming a local-moment Heisenberg model for the magnetism, can reveal information about whether an AF ground state has a planar noncollinear structure, and if the noncollinear structure is a helix or cycloid, what the pitch of the helix or cycloid is. Further magnetic neutron diffraction measurements are needed to test our hypotheses for the composition dependence of the ground state magnetic structure of the orthorhombic  $\text{Lu}_{1-x}\text{Sc}_x\text{MnSi}$  system.

### Acknowledgments

We thank Srinivasa Thimmaiah for measuring the powder XRD pattern for  $\text{LuMnSi}$ . The work at Ames Laboratory was supported by the U.S. Department of Energy, Office of Basic Energy Sciences, Division of Materials Sciences and Engineering. Ames Laboratory is operated for the U.S. Department of Energy by Iowa State University under Contract No. DE-AC02-07CH11358.



---

\* Present address: Helmholtz-Zentrum Berlin für Materialien und Energie, Hahn-Meitner Platz 1, 14109 Berlin, Germany.

† johnston@ameslab.gov

<sup>1</sup> *Frustrated Spin Systems*, ed. H. T. Diep (World Scientific, Singapore, 2004).

<sup>2</sup> M. F. Collins and O. A. Petrenko, *Can. J. Phys.* **75**, 605 (1997).

<sup>3</sup> Y. Tokura and S. Seki, *Adv. Mater.* **22**, 1554 (2010).

<sup>4</sup> D. C. Johnston, *Phys. Rev. Lett.* **109**, 077201 (2012).

<sup>5</sup> S. L. Samal, A. Pandey, D. C. Johnston, and J. D. Corbett, *J. Am. Chem. Soc.* **135**, 910 (2012).

<sup>6</sup> A. Yoshimori, *J. Phys. Soc. Jpn.* **14**, 807 (1959).

<sup>7</sup> G. Venturini, I. Ijjaali, E. Ressouche, and B. Malaman, *J.*

*Alloys Compd.* **256**, 65 (1997). The right-hand ordinate of Fig. 2 should have units of emu/g instead of emu/mole as labeled (G. Venturini, private communication). The conversion of the Gaussian cgs units for magnetic moment used in Ref. 7 to the Gaussian cgs units used in our paper is  $1 \text{ emu} = 1 \text{ G cm}^3 = 1 \text{ erg/G}$ , where  $1 \text{ G} = 1 \text{ Oe}$ . See also Sec. 3.5.1 in Ref. 9.

<sup>8</sup> I. Ijjaali, R. Welter, G. Venturini, and B. Malaman, *J. Alloys Compd.* **292**, 4 (1999).

<sup>9</sup> D. C. Johnston, *Adv. Phys.* **59**, 803 (2010).

<sup>10</sup> J. Rodriguez-Carvajal, *Physica B (Amsterdam)* **192**, 55 (1993); see also [www.ill.eu/sites/fullprof/](http://www.ill.eu/sites/fullprof/).

<sup>11</sup> M. E. Fisher, *Phil. Mag.* **7**, 1731 (1962).